International Journal of Rock Mechanics & Mining Sciences 130 (2020) 104235

Contents lists available at ScienceDirect

International Journal of Rock Mechanics and Mining Sciences

journal homepage: http://www.elsevier.com/locate/ijrmms

Mechanical and hydraulic transport properties of transverse-isotropic Gneiss deformed under deep reservoir stress and pressure conditions

Mateo Acosta *, Marie Violay

EPFL, LEMR, Lausanne, Switzerland

ARTICLE INFO

Keywords:
Enhanced geothermal systems
Anisotropic rock deformation
Gneiss hydraulic transport properties

ABSTRACT

In central Europe, many geo-energy reservoirs have revealed to be hosted in transverse isotropic crystalline rock, where the rock's mechanical and hydraulic transport properties are poorly constrained. Here, we performed triaxial experiments on Cresciano Gneiss samples under realistic stress (25–40 MPa) and fluid pressure (5 MPa) conditions. We tested 5 different foliation orientations towards the major principal stress (0, 30, 45, 60, 90°). During deformation, we measured the porosity evolution and acoustic emission activity of the samples. In addition, we measured the axial permeability and P-wave velocity of the samples both during isostatic confinement and after sample failure. Our results show that the mechanical and hydraulic transport properties of transverse isotropic tight crystalline rocks can be separated into two classes. First, the mechanical properties such as onset of dilatancy, yield stress, peak strength and residual strength, follow a "U-type" anisotropy towards foliation angle, with maximum values at 0 and 90° and minima between 30 and 45°. These properties, as well as the porosity variation during deformation which follows an inversed "U-type" shape can be explained by anisotropic wing crack models. Second, the volumetric physical properties (permeability and P-wave velocity) follow a "decreasing order" shape towards foliation angle, with maximum values at 0° decreasing to the minimum at 90°. These properties show a high dependence on the stress state and the wave path. We discuss the implications of these results for deep geothermal energy prospection, and for reservoir stimulation and operation.

1. Introduction

The clean and sustainable development of Enhanced Geothermal Systems (EGS) and other geo-energy activities needs an appropriate knowledge of host rock mechanical and hydraulic transport properties in order to assess the economic viability of the sub-surface reservoirs. In central Europe, many EGS reservoirs are to be hosted at depths of 2.5–5 km in the fractured crystalline basement.[1] Recent experiments in underground research laboratories[2–5] have shown that the targeted crystalline basement can be strongly foliated, resulting in anisotropic (or transverse-isotropic) mechanical and hydraulic transport properties. A comprehensive understanding across scales of the mechanical behavior and hydraulic transport in such foliated basement rock is thus necessary for reservoir design and operation.

At the laboratory scale (tens of centimeters), the mechanical behavior of crystalline rock has received a great interest in the rock mechanics community but mostly for isotropic rock. The most popular model of strength anisotropy considers the criteria for slip on a single plane of weakness,[6] but does not predict damage initiation and progression, fundamental parameters for hydraulic transport in rock and estimation of reservoir integrity.[7] On the other hand, fracture mechanics models[8–13] state that brittle failure of rock materials can be described first by the nucleation of pre-existing cracks (e.g flaws in the rock microstructure) and their ensuing growth and propagation until the cracks are large enough to interact with each other. As wing cracks propagate, the increase in tensile stresses at their tips can result in macroscopic dilatancy (e.g porosity increase). Following this phase, the wing cracks can interact with each other's stress fields,[12] ultimately leading to instability and macroscopic failure. At failure, anastomosing shear bands are formed over which stress is released with increasing strain.[14] Such models are particularly suited for transverse isotropic rock because they provide a physical basis to study rocks containing preferentially oriented micro cracks (e.g defects) which in turn control the mechanical response of the matrix and the evolution of damage within it.[15]

The initial porosity of the subsurface rock and its evolution as response to external forcing has direct effects on i) the mechanical properties of the reservoir[7,13,16] and ii) the hydraulic transport

* Corresponding author.
E-mail address: mateo.acosta@epfl.ch (M. Acosta).

https://doi.org/10.1016/j.ijrmms.2020.104235
Received 11 November 2019; Received in revised form 24 January 2020; Accepted 24 January 2020
Available online 9 April 2020

properties of the reservoir rock.[7,17,18] The porosity change during deformation in isotropic crystalline rocks has been extensively studied under room temperature[9,19–22] and at high temperature.[23,24] Such studies have shown that, in the brittle domain, the development of porosity in isotropic granite is due to the opening of stress induced cracks parallel to the direction of the major principal stress (e.g wing cracks) but few studies have dealt with porosity change under transverse isotropic conditions.[15] In addition, the total pore volume of the rock matrix is not the only factor influencing the mechanics and fluid transport properties of crystalline reservoirs. Indeed, faults and their surrounding damage zones constitute mechanically 'weak' and highly permeable structures if compared to intact rock.[7,25,26] Therefore, the main parameters that control fluid flow in crystalline rocks are rather related to the geometry and connectivity of the fractures.[17,18,27–32] Such parameters remain poorly constrained in transverse isotropic rock.[4,5]

Estimations of the fluid flow in underground reservoirs can be done through the use of intrinsic and apparent permeability of the intact, as well as the damaged and fractured rock. Again, many studies have investigated the permeability of intact and faulted isotropic crystalline rocks[23,24,34–42] but the permeability of foliated crystalline rocks has received less attention.[5,43–49,51] In the case of transverse-isotropic rock fabric, most developments have been made to understand the permeability tensor[45] but in practice the tensor is difficult to determine. Assuming transverse isotropy, the apparent permeability can be measured in several directions towards the main foliation axis and can then be input into reservoir models that take into account anisotropy of permeability due to i) foliation induced anisotropy and ii) fracture induced anisotropy[7] in order to estimate injection/extraction rates in the long term reservoir operation.

Here, we present a comprehensive study of the mechanical and hydraulic transport properties of strongly foliated, transverse-isotropic gneiss as a function of the foliation angle towards the applied major principal stress. The samples are representative of the central European crystalline basement. In section 2, we describe the experimental methodology used for this study. Then, in section 3, we present the experimental results of i) the evolution of P-wave velocity and apparent permeability of the samples during isostatic confinement ii) the mechanical results of tri-axial deformation as well as the evolution of porosity and acoustic emissions up to failure and iii) comparative results of P-wave velocity and permeability of intact and failed samples under high (residual) and low (isostatic) differential stress. In section 4, the mechanical results are discussed along with their implications for reservoir mechanics. Section 5 is aimed to discuss hydraulic transport properties of EGS and other geo-energy reservoirs. Finally, the results are discussed with respect to reservoir prospection, stimulation and operation in section 6 and a summary of the results and major conclusions are given in section 7.

2. Materials and methods

2.1. Starting samples

The experimental samples were Cresciano Gneiss (*CGn*) right circular cylinders of ~36 and ~72 mm diameter and length respectively. *CGn* (Or gneiss Leventina type II[52]) is a strongly foliated and lineated gneiss of granitic composition (~42 ±5% Quartz ~22 ±2% Alkali-feldspar ~2.4 ±0.5% Plagioclase ~30 ±4% Biotite ~9 ±0.5% Muscovite and accessory minerals) typical of the upper continental crust. The foliation bands consist of successive occurrence of Quartzo-Feldspatic layers and Micaceous layers. A detailed petrographic analysis of *CGn* as well as the locations where it can be extracted can be found in Refs. [52] This material is particularly representative of foliated crystalline rock reservoirs that are set to host deep geothermal activities in central Europe.[4,5] In addition, this material is suitable for laboratory work due to its low alteration, strong homogeneity, fine grain (~0.03–3 mm average grain size), simple mineralogy and well developed transverse-isotropy (Fig. 1b–c). The cylinders were cored in five directions of the core's long axis with respect to the principal anisotropy axis of a single rock block of well-defined gneissic banding orientation (Fig. 1a–b). Sample orientations can be described by the angle β that their long axis makes with the foliation plane (Fig. 1a). In triaxial deformation experiments, the foliation angles tested were 0°, 30°, 45°, 60°, and 90°. A summary of the performed experiments is given in Table A1. In addition to experiments performed on *CGn*, experiments for comparison were performed on an isotropic crystalline rock (LaPeyratte granite[53,54]) (labelled from now on as LPG).

2.2. Experimental set-up

Tri-axial deformation experiments were performed in an oil-medium Hoek-cell under a hydraulic press (Fig. 1d) of the Laboratory of Experimental Rock Mechanics (LEMR) at EPFL. The Hoek cell can support a confining pressure of 70 MPa (+- 50 kPa) with $\sigma_3 = \sigma_2$.

The axial deformation was transmitted through stainless steel anvils that can hold a maximum axial stress (σ_1) of 1 GPa (+- 100 kPa) for samples of 36 mm diameter.[55] Under this configuration, axial stress was calculated as $\sigma_1 = \frac{F_{ax}}{S}$ with F_{ax}, the measured axial force and S the sample's cross section. Radial stress (σ_3) was measured from pressure sensors located in the servo-controlled radial pump. Differential stress was computed as $\Delta\sigma = \sigma_1 - \sigma_3$. Displacement ($d$) was computed from the mean of two linear displacement sensors (~1 μm resolution) located between the top and bottom anvils. Strain was computed as $\varepsilon(t) = \frac{d(t)-d(0)}{L}$, L being the initial sample's length, and $d(0)$ the measured displacement at start of deformation. The axial stiffness of the column is 1000 kN mm^{-1}. Pore fluid pressures and volumes were controlled through 2 pressure/volume controllers connected to the top and bottom anvils (Fig. 1d). They have a capacity of 200 cm^3 (+-1 mm^3) in volume and 30 MPa (+- 1 kPa) in pressure.

For passive acoustic emission (AE) monitoring, two wideband (200–1150 kHz) piezoelectric transducers were placed in the top and bottom anvils (Fig. 1d). The signal was amplified to 40 dB through in-line preamplifiers. AE's were recorded under a trigger set-up in order to record events of amplitude higher than 0.056 V (and avoid logging background noise measured at 0.032 V) at 200 MHz monitoring rate and 1 MHz sampling rate. The AE catalogue was synchronized in time (at millisecond resolution) with the mechanical and hydraulic data during rock deformation (Fig. 2 grey curve).

To perform active measurement of ultrasonic wave velocity, an additional set-up was composed of an arbitrary wave generator (Opmux by Optel ultrasonic technology) connected to the top sensor (emitter) and a 2 channel digital oscilloscope (Handyscope by TiePie Engineering) connected to the top (emitter) and bottom (receiver) sensors. The oscilloscope was sampled at 200 MHz in time windows of 100 μs When needed, measurement was manually switched between active and passive acoustic monitoring set-ups. For active P-wave velocity measurements, the travel time of an elastic pulse of 1 μs duration (e.g 1 MHz frequency) and 400V amplitude through the rock sample was measured and divided by the effective travel length. Corrections were made for the travel time in the anvils and for strain during mechanical loading. The wave arrival times were picked by automatic P-wave arrival detection of an increase of the time integral of the squared voltage with a threshold of 5.10–3 V^2 s in time windows of 0.25 μs

Porosity evolution was monitored during triaxial deformation through the fluid volume/pressure controllers (Fig. 1d). Volume change of the loading system during deformation is here neglected due to the high stiffness and low compressibility of the top and bottom anvils. Fluid pressure was imposed constant during deformation, therefore, the sum of volume changes in top and bottom controllers corresponds to the volume change inside the sample. Permeability was measured in our experiments during i) isostatic loading, ii) after sample failure and iii) after unloading. Because the permeability of an anisotropic rock is a

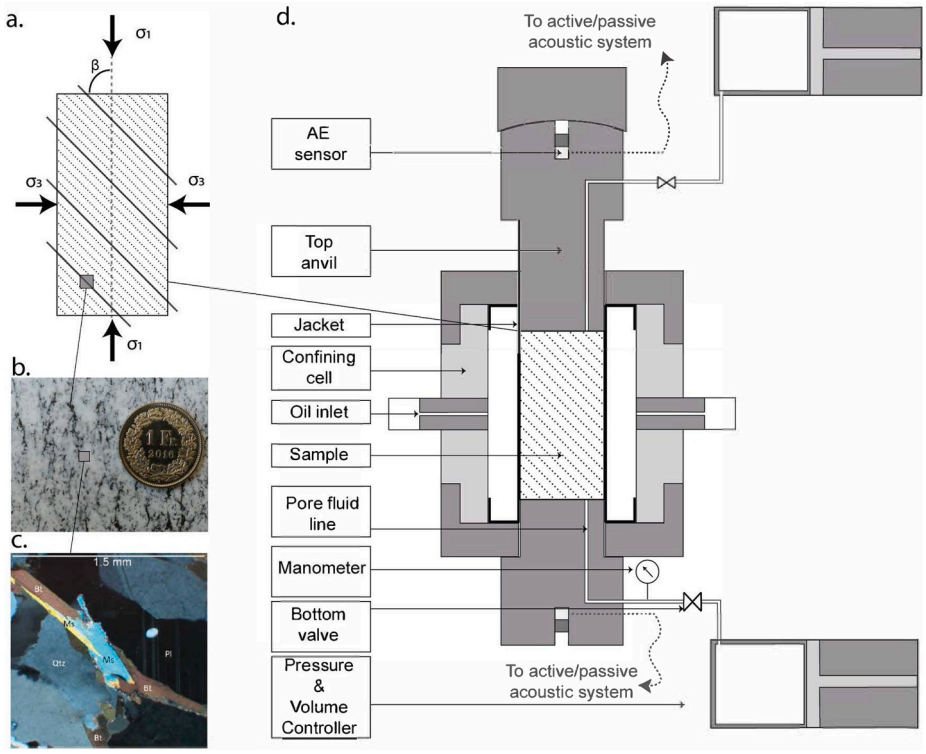

Fig. 1. Experimental samples and set-up. **a** Sketch of the transversely isotropic sample, the angle between the major principal stress axis (dotted vertical line) and the foliation orientation (grey lines) is defined here as β. **b** Photograph of the transversely isotropic Gneiss sample, 1 chf for scale. **c** Cross polarized optical micrograph of the un-deformed experimental sample. **d** Sketch of the deformation apparatus (modified after [Ref 55]).

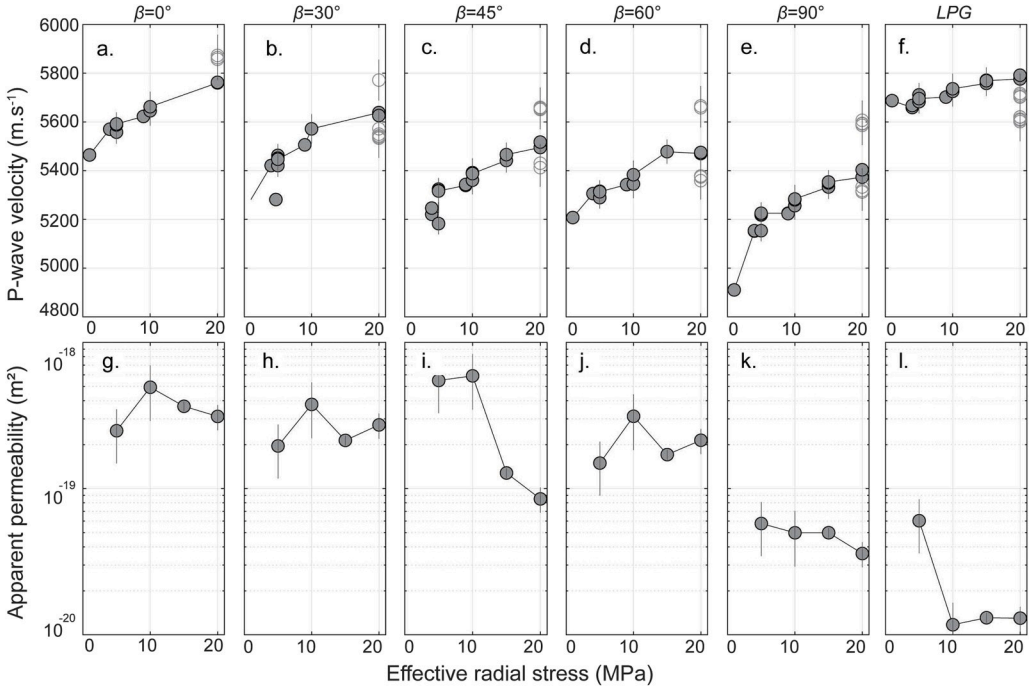

Fig. 2. P-wave velocity and apparent permeability during isostatic confinement. **a-f.** P-wave velocity measurements function of isostatic effective confinement (σ_1' = σ_3'). **g-l.** Permeability measurements function of isostatic effective confinement. Titles show the foliation orientation angle towards the vertical axis.

tensorial quantity,[45,51,56] the axial permeability measurements at each foliation orientation will be treated as "apparent permeability" throughout the text.

To measure permeability in our experiments, two different methods were used. If the apparent permeability was higher than 10^{-18} m^2, the steady state flow method was used. This method consists in imposing a differential pressure (here 0.2 MPa) between the top and bottom ends of the sample until a steady state volume flow rate is reached. Darcy's law was applied to retrieve the sample's intrinsic permeability as $k = -Q$.

$\frac{\mu.L}{S.\Delta P}$ where Q is the volumetric flow rate, μ water's dynamic viscosity, L and S the sample's length and cross section respectively and ΔP the imposed pressure gradient. On the other hand, if permeability was lower than 10^{-18} m^2, the oscillatory fluid flow method[57–61] was used. This method consists in studying the transmission of an oscillating pressure wave from the sample's top to bottom. The received pressure wave presents a phase shift (θ) and an attenuation in amplitude with respect to the emitted pore pressure wave. Using the analysis of this technique by Bernabé et al.[61] the phase shift (θ) and amplitude ratio A can be directly linked to the sample's storage capacity (β_s) and its intrinsic permeability (k) respectively. Note that when using the oscillatory pressure pulse method, a valve connected right after the bottom anvil (Fig. 1d) was closed in order to reduce as much as possible the downstream volume and improve the accuracy of the method.[59,61] In that case, the pressure was measured through a calibrated manometer (1 kPa resolution). The use of this technique to estimate permeability presents several advantages: (i) in low permeability rocks, it considerably reduces measurement time because there is no need to achieve steady state volume flow rate. (ii) The measurement of permeability remains accurate even when storage capacity cannot be resolved (for details see Ref. [61]) and (iii) it allows measurement of permeabilities as low as 10^{-22} m^2.

2.3. Loading procedure

The samples were first pre-saturated in a vacuum chamber with de-ionized, de-aerated water for a minimum of 24 h. Then, the samples were set into the triaxial deformation set-up described above. Following this, the procedure was as follows: Stage 0, Isostatic loading: Samples were taken to $\sigma_1 = \sigma_3 =$ 25 MPa through steps of 5 MPa at rates of 0.1 MPa s^{-1} p_f was imposed to 5 MPa. At each confinement step, P-wave velocities and permeability were measured. Stage I, Axial Deformation: σ_3 and p_f were kept constant. The axial piston was advanced at a constant displacement rate resulting in a constant strain rate of $\dot{\varepsilon_{ax}} = 10^{-6}\ s^{-1}$ until sample failure. The axial piston was kept in position and P-wave velocity and permeability measurements were performed. Stage II: σ_3 was increased at 0.1 MPa/s to 40 MPa through steps of 5 MPa. At each confinement step, the axial piston was advanced at a strain rate of $\dot{\varepsilon_{ax}} = 10^{-6}\ s^{-1}$ until reaching a new steady state axial stress value. Stage III, Unloading: After the last confining pressure step the samples were unloaded by lowering the axial piston at constant displacement rate of 0.007 $mm.s^{-1}$ until σ_1 reached 25 MPa (e.g isostatic confinement). P-wave velocity and permeability measurements were performed. The samples were then unloaded isostatically and retrieved for post-mortem study.

2.4. Experiment reproducibility and error estimation

To study the reproducibility of our experiments, a second experiment under nominally identical conditions was conducted for a foliation angle of 45° (Fig. 4c,i, grey lines). The result shows that an intrinsic error due to sample variability exists. This is due to the inevitable changes in sample structure and mineralogy from sample to sample. From the reproducibility experiment, the error is estimated to 9% in terms of stress and 11% in terms of porosity change. The errors regarding P-wave velocity and permeability are estimated to be stress and failure dependent and range from 1.7 to 3.7% regarding P-wave velocities and from 15 to 62% regarding apparent permeability. The errors estimated due to sample variability are estimated to be the largest errors in these experiments and are thus reported in all the figures and calculations.

3. Experimental results

3.1. P-wave velocity and apparent permeability during isostatic loading

P-wave velocities (V_p) and apparent permeability (k_{app}) of the samples were measured during confinement steps. Fig. 2a–f shows V_p in our samples during isostatic loading ($\sigma_1' = \sigma_3'$). At $\sigma_3' = 20$ MPa, V_p decreased from 5762 to 5403 m s^{-1} respectively for angles between $\beta = 0$ and 90°. With increasing effective stress, the P-wave velocities increased for all foliation orientations. The increase was the lowest at $\beta = 0°$ (~5.5% increase) and the highest at $\beta = 90°$ (~10.1% increase). For comparison, the P-wave velocities in isotropic granite were the highest (~5800 m s^{-1}) with the smallest increase (0.9%) (Fig. 2f).

Fig. 2g-l shows the apparent permeability (k_{app}) in our samples during isostatic ($\sigma_1' = \sigma_3'$) confinement steps. At $\sigma_3' = 20$ MPa, k_{app} decreased from $3.12.10^{-19}$ to $0.57.10^{-19}$ m^2 for angles $\beta = 0$–90°. At all foliation orientations, the permeabilities usually decreased with increasing effective stress. The decrease was the lowest at $\beta = 0°$ and the highest at $\beta = 90°$. For comparison, the permeability of a fully isotropic granite is ~$0.12.10^{-19}$ m^2 between 10 and 20 MPa effective confinement (Fig. 2l).

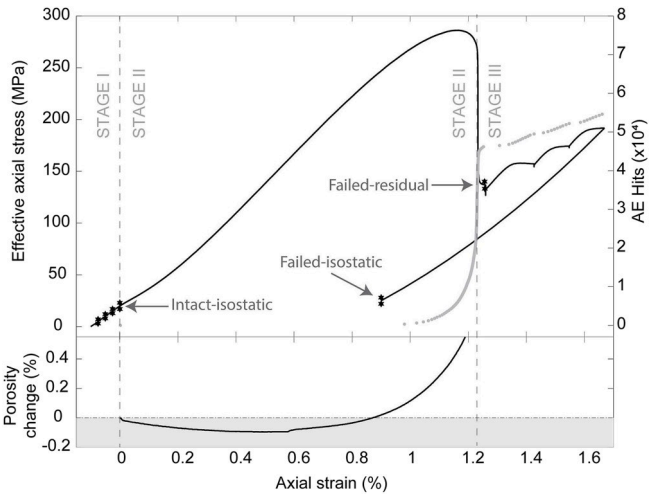

Fig. 3. Typical deformation experiment. **Upper panel.** Effective axial stress (black line) and cumulative acoustic emission arrivals (grey dots) function of axial strain. Arrows indicate where the measurements of permeability and P-wave velocity corresponding to Fig. 5 were performed. **Lower panel.** Porosity change (negative corresponds to compaction (grey area) and positive to dilation) function of axial strain.

3.2. Triaxial deformation

During triaxial deformation, and for all sample orientations, the increase in differential stress was first nonlinear with increases in strain. In terms of porosity change (lower panel of Fig. 3), the deformation was usually compactant until the end of this phase. Then, an elastic loading phase followed with a linear increase in differential stress with increasing strain. After this, the rise in differential stress became nonlinear and the porosity change switched from compaction to dilatancy due to crack initiation at the stress level C'.[9,15,62] This stage lasted until the peak strength of the specimen was reached. Then, differential stress decreased to a residual value, defining a stress drop. The volumetric deformation sharply increased as well as the total number of acoustic emissions. The sample's failure was accompanied by the creation of anastomosing shear bands.

Stress strain curves (black lines) and AE activity (grey dots) during triaxial deformation experiments are presented in Fig. 4a–f. Porosity evolution corresponding to fluid pressurized experiments are shown in Fig. 4g-l. Compilation of mechanical data corresponding to these experiments is presented in Fig. 7.

Fig. 4 shows that samples at $\beta = 0°$ failed at a peak stress ~300 MPa. At $\beta = 30°$ and 45°, the peak stresses were the lowest (~160 MPa). With increasing β, the samples were stronger (~200 MPa at 60°) and the

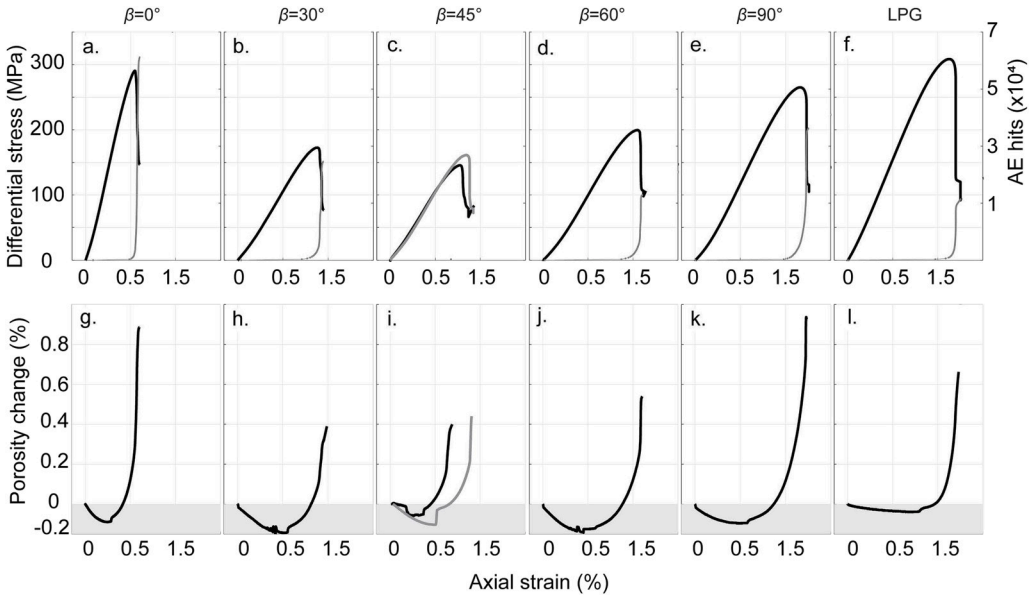

Fig. 4. Triaxial deformation results. **a-f**. Fluid pressurized experiments at 25 MPa confining pressure and 5 MPa pore fluid pressure. Black lines represent Differential stress vs. Axial strain. Grey dots show the number of AE recorded during the experiment. **g-l**. Porosity change vs. Axial strain. Grey area (e.g negative porosity change) represents compaction.

differential stress needed for failure was largest at 90° (~280 MPa). For comparison, a fully isotropic granite had a peak strength ~310 MPa (Fig. 4f). Overall, the peak stress followed a U-shaped curve with increasing foliation angle (Fig. 7).

Similar trends were observed with the total number of acoustic emissions at peak stress (grey dots) with a maximum recorded at $\beta =$ 0 and 90° (~75e3 and >50e3 respectively). The minimum cumulative AE number was recorded at $\beta = 45°$ (<500 AE's).

Regarding porosity change (Fig. 4g-l), the experiments at $\beta = 30°$ and 60° showed the maximum compaction (~14%) prior to the onset of dilatancy C'. Experiments at $\beta = 0$ and 90° presented intermediate compaction (~7 -10%) at C′ and the experiment at $\beta = 45°$ presented the minimum value at C' (5%). At peak stress, the samples presented a total porosity change of 0.29, 0.075, 0.41; 0.20 and 0.43% for angles 0, 30, 45, 60 and 90° respectively (Table A1).

3.3. P-wave velocity and apparent permeability of failed samples

V_p and k_{app} after sample failure were measured i) when the residual friction of the samples was reached (Fig. 5, grey triangles) and ii) after the axial force was decreased to isostatic loading conditions ($\sigma_1' = \sigma_3' = 20$ *MPa*; Fig. 5, grey circles). These measurements are related to i) the sample directly after failure with a high deviatoric stress and ii). the failed sample but this time under isostatic conditions (e.g with 0 MPa

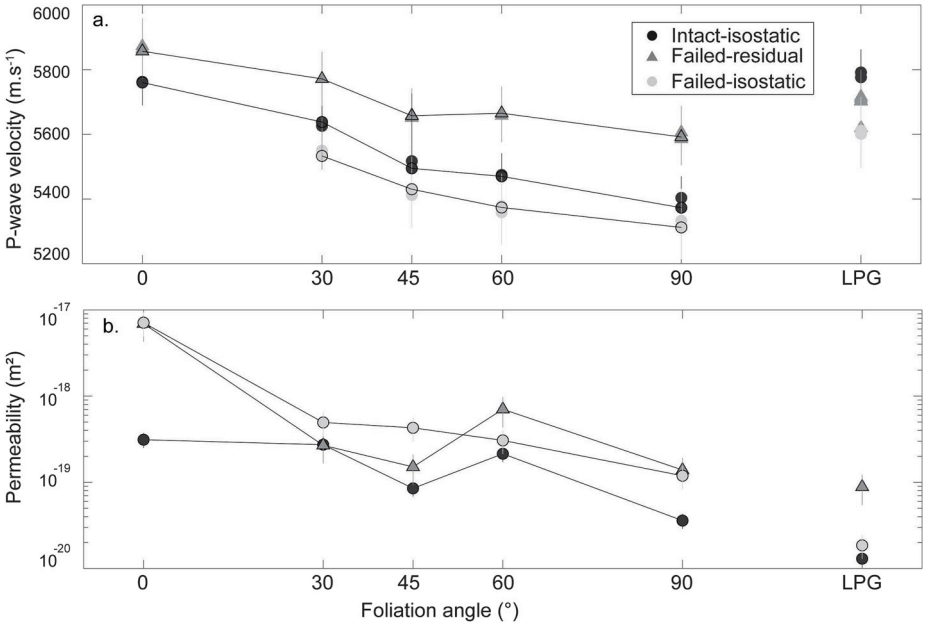

Fig. 5. Physical properties of failed samples. **a**. P-wave velocity versus sample orientation. **b.** apparent permeability versus sample orientation. Black circles correspond to measurements of intact samples under isotropic stress state ($\sigma_1' = \sigma_3'$=20 MPa). Grey triangles correspond to failed samples at residual stress state ($\sigma_1' >> \sigma_3'$). Grey circles correspond to measurements of failed samples under isotropic stress state ($\sigma_1' = \sigma_3'$=20 MPa).

deviatoric stress). In Fig. 3, the locations where these three measurements were made are placed on the example stress-strain curve.

Fig. 5a shows that V_p decreased with increasing β under all conditions (intact-isostatic (black circles); failed-residual (grey triangles); and failed-isostatic (grey circles)). In addition, a systematic increase of ~2% between intact-isostatic ($\sigma_1' = \sigma_3' = 20$ MPa) and failed-residual ($\sigma_1' > > \sigma_3'$) conditions was observed. Comparing failed-residual ($\sigma_1' > > \sigma_3'$; Fig. 5a, grey triangles) and failed-isostatic ($\sigma_1' = \sigma_3'$; Fig. 5a, grey circles) conditions, there was a reduction of more than 4.5% in V_p. The reduction was the largest at $\beta = 90°$. Finally, comparing intact-isostatic (black circles) and failed-isostatic (grey circles) conditions, the reduction of V_p was ~1.2%. For comparison, a fully isotropic granite, presented V_p ~5800 m s^{-1} at intact-isostatic, ~5700 m s^{-1} at failed-residual and ~5600 m s^{-1} at failed-isostatic conditions.

Fig. 5b, shows that k_{app} decreased when increasing β from 0 to 45°. Then, a local increase in k_{app} was observed at 60° and reached a minimum at 90° for all conditions (intact-isostatic (black circles); failed-residual (grey triangles); and failed-isostatic (grey circles)). Comparing intact-isostatic and failed-residual conditions, the largest increase of k_{app} occurred at $\beta = 0°$ (>10 times increase) while at $\beta = 30°$, no increase was observed. At angles 45, 60 and 90°, the increase in permeability was of 2.5–4 times. Comparing failed-residual (Fig. 5b, grey triangles) and failed-isostatic (grey circles) conditions, an increase of k_{app} of 23, 1.7 and 2 times was observed for $\beta = 0$, 30 and 45°. Finally, at 60° a reduction of half in k_{app} was observed and at $\beta = 90°$ no change in k_{app} was recorded. For comparison, the permeability of an isotropic granite increased after failure (from ~$0.05.10^{-19}$ to $0.9.10^{-19}$ m s^{-1}) and decreased (to ~$0.1.10^{-19}$ m^2) after reduction of the differential stress.

3.4. Macro-structure of failed samples

All samples failed by formation of macroscopic shear bands. Such faults were formed by anastomosed microscopic cracks.[15,63,64] At $\beta = 0°$ (Fig. 8a), the failed sample presented several non-connected fractures oriented sub-parallel to the major principal stress (at angles ~7–15°, Fig. 6g). For $\beta = 30$, 45, and 60°, the fracture orientations were ~30+-3° towards the major principal stress. Note that at $\beta = 30°$ (Fig. 6b), the fracture occurred following one single biotite plane whereas at $\beta = 45°$

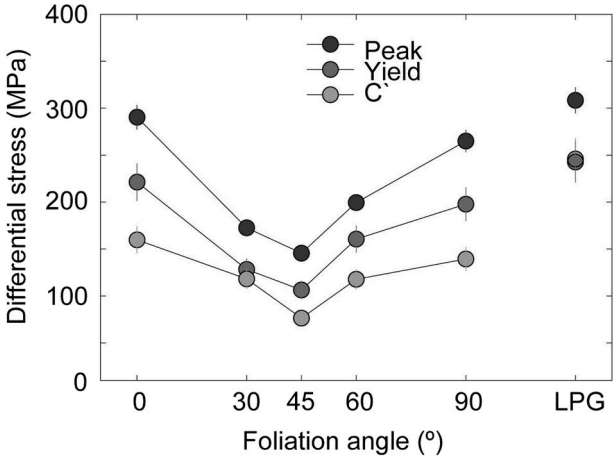

Fig. 7. Mechanical strength: Stress at onset of dilatancy, yield stress, and Peak strength versus foliation angle.

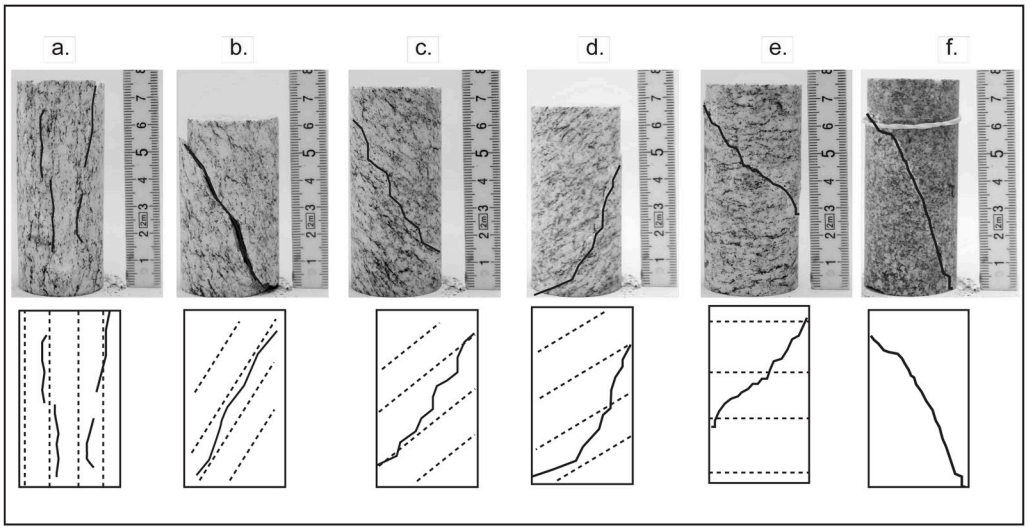

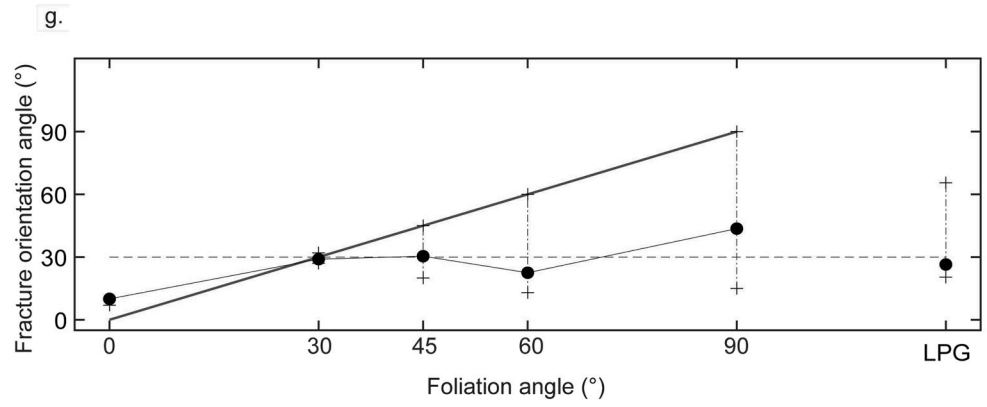

Fig. 6. Post-mortem structures and fracture orientation. **a-f.** Photographs and sketches of the failed samples. In the photographs, black lines show the fractures. In the sketches, grey dotted lines show the principal foliation and black lines show the fracture. **g.** orientation of the failure planes versus foliation angle with respect to the major principal stress. Grey line represents (1:1) angles. Dotted line represents 30° fracture orientation angle. Errorbars show the minimum and maximum orientations of fracture fragments.

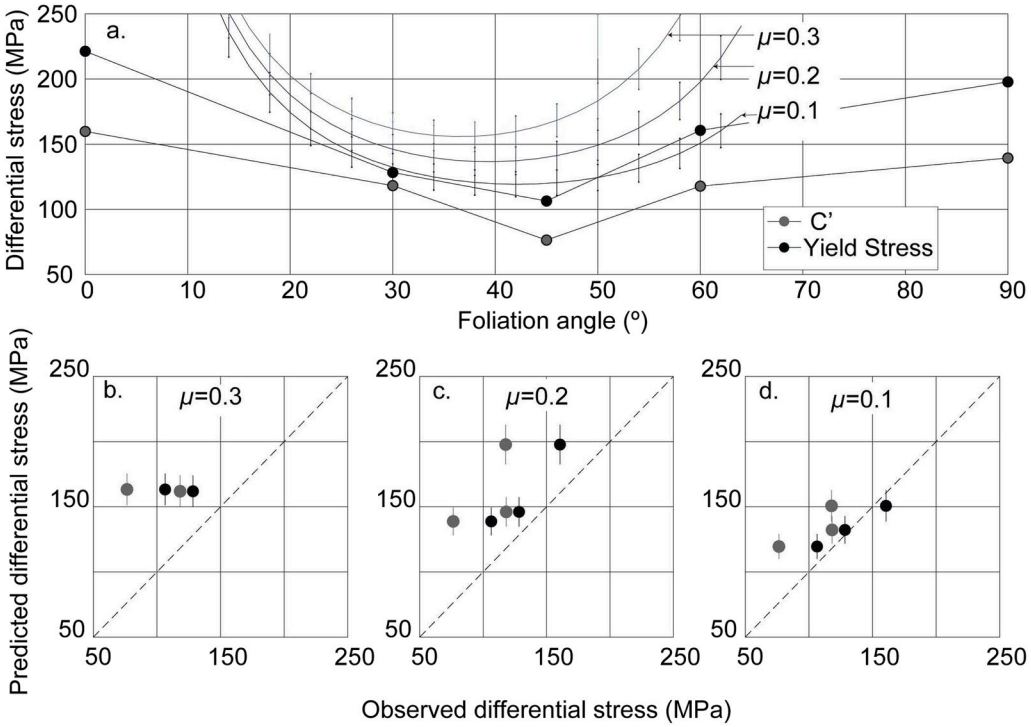

Fig. 8. Micromechanics of the onset of damage. **a**. Differential stress at the onset of damage function of foliation orientation. Grey lines show the prediction of differential stress at the onset of crack propagation from the model of Rawling et al. [15] with different internal friction angles. Data from the experiments on *CGn* are presented to see the correspondence with the model. **b,c,d.** Differential stress at the onset of micro crack propagation predicted by the model as function of the observed differential stress (at C′ and at yield stress) with internal friction of 0.3, 0.2, and 0.1. All the models are computed with a normalized fracture toughness $\frac{K_{1c}}{\sqrt{\pi.a}}$ ~60±5 MPa.

(Figs. 6c) and 60° (Fig. 6d), the fracture had "en-echelon" structure with the fracture jumping from one biotite layer to another through failed Quartzo-Feldspatic layers. Finally, at $\beta = 90°$ (Fig. 6e), the failed structure presented one single fracture oriented at ~43° towards the major principal stress. For comparison, the post-mortem structure of isotropic granite (Fig. 6f) showed a single fracture ~26° to the major principal stress.

Note that in all cases, the orientation of foliation layers exerted some control over the fracture orientation and development.[15,63–65]

4. Mechanics of brittle failure: damage initiation, faulting and residual strength

For the development and exploitation of geothermal reservoirs in transverse isotropic rocks, it is of interest to know i) at which stress damage initiates in the rock matrix because damage is expected to control rock hydraulic transport properties.[26] ii) at which stress and how will the matrix fail, this can help evaluation of the integrity of the reservoir, and iii) the strength of preexisting faults since they control the overall mechanics of the reservoir. In the following discussion, we first summarize the mechanical results, then, a prediction for the onset of damage based on a micro mechanical model will be proposed. Following this, a detailed study of the failure mechanisms of *CGn* will be discussed. Finally, the mechanics of residual friction on fractured samples will be studied.

For Cresciano Gneiss, as is the case for weakly anisotropic rocks[13] the stress at the onset of dilatancy, yield stress and peak strength (Fig. 7) versus foliation orientation curve is concave upward on the whole range of foliation orientations.[15,63–65] It does not show 'flat shoulders' as would be predicted by the single plane of anisotropy theory[6] on strongly bedded or singly jointed rocks and can therefore be defined as "U-type" mechanical anisotropy.[66,67] The maximum values of all these mechanical properties is located at β ~0 and 90°. At those angles, the rock's strengths are close to that of an isotropic granite. In accordance, the minima of all mechanical properties can be found at $\beta \sim 45°$.

4.1. Onset of damage

Based on microstructural observations, Rawling et al.[15] have modified the isotropic model of Ashby and Sammis[11] for nucleation and propagation of wing cracks to propose a crack nucleation criterion in anisotropic rocks. There, the authors assume that the principal stresses are related by $\sigma_1 = m_d.\sigma_3 + \sigma_{cd}$, with σ_1 and σ_3 the axial and radial stresses applied on the crack at the onset of crack nucleation and propagation. Then, in transverse-isotropic conditions (similar to those in our study), frictional slip will first be activated in the weaker minerals (biotite in our case[68]) when the foliation has a suitable orientation (β) towards the major principal stress. In such case, the slope m_d and intercept σ_{cd} (noted m and c in Rawling et al.[15]) parameters can be written as:

$$m_d = \frac{\sin 2\beta + \mu.(1+\cos 2\beta)}{\sin 2\beta - \mu.(1-\cos 2\beta)}$$

and

$$\sigma_{cd} = \frac{\sqrt{3}}{\sin 2\beta - \mu.(1+\cos 2\beta)}.\frac{K_{1c}}{\sqrt{\pi a}.}$$

where μ is the friction coefficient, and $\frac{K_{1c}}{\sqrt{\pi a}}$ is the normalized fracture toughness related to the nucleating cracks (of half-length a) this term replaces the 'cohesive' term in a classical Mohr-Coulomb failure approach. Note that this model can only be applied to intermediate foliation orientations ($0 < \beta < \tan^{-1}\left(\frac{1}{\mu}\right)$) because when the weak materials are oriented outside this range, biotite will typically deform by kinking or faulting rather than by frictional slip and will thus increase the crack's strengths (e.g Section 4.2 of Rawling et al.[15]) resulting in physically unrealistic values predicted by the model.

Using this model, we observe (Fig. 8) that friction coefficients μ ~0.1–0.2 are needed to correctly predict the experimental data. This is in agreement with previous measurements, where static friction coefficient of biotite was estimated between ~0.13 and 0.31.[68] A low normalized fracture toughness (e.g. the cohesive term of the failure

criterion) of $\frac{K_{1c}}{\sqrt{\pi a}}$~60 +- 5 MPa is also needed to explain the results on *CGn* with respect to the results of Rawling et al.[15] where $\frac{K_{1c}}{\sqrt{\pi a}}$~86 +-6 MPa. Such differences can arise from several facts: i) The experiments presented in this study were performed at $\sigma_3' = 20$ MPa, while those of Rawling et al.[15] were performed at $50 < \sigma_3 < 300$ MPa. It is possible that the mechanical processes leading to failure are rather friction dominated in our experiments (low normal stress acting on the wing cracks) and toughness dominated in those of Rawling et al.[15] (high normal stress). ii) It is also likely that, because *CGn* (~30% Biotite) is slightly different in composition to Four-Mile Gneiss (~12 ± 5% Biotite), the normalized fracture toughness can be lowered. Further experiments as well as detailed comparative petrographic analyses are needed to constrain the reasons for such differences and are out of the scope of this study.

4.2. Sample failure

From post-mortem sample analysis, we have seen that at $\beta = 0°$, the main fracture was sub-vertical, at 30° it followed the biotite layer, while at 45, 60 and 90°, the fracture presented an en-echelon structure. Based on existing literature, these results will now be discussed.

The micro mechanics of failure predict that after wing-crack nucleation under macroscopic compressive load, an increase in tensile stresses at the crack tips can result in macroscopic dilatancy. Following this phase, the wing cracks can interact with each other's stress fields, ultimately leading to micro crack coalescence and macroscopic failure.[10,11,13,15] Observation of the post mortem structural characteristics are in accordance with these results (Fig. 6) as follows: i) At orientations $\beta = 0°$, biotite layers deform by kinking due to the low angle towards the major principal stress as stated in previous works in transverse isotropic crystalline rock.[15,63,64] At this orientation, biotite grains are not favorably oriented for slip with respect to the applied stress field, resulting in high peak strength and low angle fractures in the post-mortem structure (Fig. 6a). ii) At $\beta = 30°$, the biotite grains and layers are the most favorably oriented for slip, reason why the failure plane follows almost flawlessly the orientation of one given micaceous plane (Fig. 6b). In accordance, yield and peak stresses, were lowest at $\beta = 30°$. iii) At orientations $\beta = 45$ and 60°, the "en-echelon" structure of the fractures have been previously related to the nucleation and propagation of wing cracks originating at the tips of biotite grains. Such wing-cracks generate tensile stress concentrations on Quartz and Feldspath minerals allowing the fractures to "jump" from one biotite layer to the next.[15] For these reasons, at $\beta = 45$ (Figs. 6c) and 60° (Fig. 6d), yield and peak stresses remained low. Finally, at $\beta = 90°$ (Fig. 6e) the biotite layers acted as barriers to the fracture propagation.[15] In this case, the biotite layers deformed mostly by faulting, justifying high values of the onset of dilatancy, yield stress and, and peak stress. For comparison, in isotropic Granite, peak strengths were close to the case where $\beta = 0°$.

4.3. Residual friction

Study of the residual frictional failure envelope can bring information on rock behavior once faults have already formed.[13,69] It is therefore of importance to the mechanics of underground reservoirs because they are mostly controlled by faults and joints.[70] The mechanical response of the newly formed fractures (in failed samples) is composed of a sliding component (frictionally dominated), and a fracturing component (fracture dominated or 'cohesive') as thoroughly described in Ref. 69. The failed sample is therefore expected to follow a residual failure criterion usually expressed as $\tau = c_r + \mu_r.\sigma_n'$ with c_r the residual cohesion and μ_r the residual friction. The residual frictional stress of the failed samples at $\sigma_3' = 20$–30 MPa are presented in Fig. 9a. From those values, the parameters c_r, and μ_r were estimated from the failure criterion in the (σ_1', σ_3') plane where the residual axial stress at failure can be expressed as $\sigma_1' = m_r \cdot \sigma_3' + \sigma_{cr}$. Then, we get $c_r = \frac{\sigma_{cr}}{2.\sqrt{m_r}}$ and $\mu_r = \tan\left(\text{asin}\left(\frac{m_r-1}{m_r+1}\right)\right)$. The residual friction angle (Fig. 9b left axis) showed again a "type-U" anisotropy with maxima of ~37° at $\beta = 0°$ and minima of ~25° at $\beta = 45°$. For comparison, isotropic granite had a residual friction angle ~32° being an intermediate value between the range of β in *CGn*. The residual cohesion (Fig. 9b right axis) presented again a maximum ~22 MPa at $\beta = 0°$ and a minimum ~5 MPa at $\beta = 30°$. Nevertheless, with increasing angles from 45 to 90°, c_r was close to constant (~20 MPa). This value was similar to the c_r of isotropic granite. It is interesting to notice that, while the residual friction angle follows again a clear U-type anisotropy, the residual cohesion seems to reach a plateau for angles 45, 60, and 90°. At all these angles β, the fractures followed an "en-echelon" structure probably the reason why the residual cohesion was similar on these failed surfaces.

5. Hydraulic transport and seismic properties of transverse isotropic rock

In order to calculate an underground reservoir's fluid extraction/injection capacity, it is of outmost importance to properly assess the porosity and permeability evolution of the reservoir rock in response to stress changes during stimulation and operation. The following discussion will first focus on the porosity changes and acoustic emission surges during triaxial deformation after the initiation of damage. Then, the effects of confinement pressure and brittle failure on permeability and P-wave velocities will be discussed.

5.1. Porosity changes and acoustic emission activity prior to macroscopic faulting

It is accepted that inelastic volume changes (e.g irreversible porosity change) during rock deformation are a proxy for the evolution of its microstructure.[13] In particular, in the brittle regime, dilatancy in compact rock occurs when it has undergone irreversible damage due to the nucleation and propagation of micro cracks.[9,15,22–24] Acoustic emission monitoring can bring crucial information on micro crack propagation (and therefore damage) inside the confined rock samples because their dynamics are usually correlated with volumetric and inelastic deformation during faulting.[71,72] It is in this sense that the acoustic emission activity and porosity changes (e.g volumetric deformation) in our experiments will be discussed together in this subsection.

The cumulative number of AE's follow a concave upward shape at intermediate foliation orientations ($\beta = 30$,45, and 60°) (Fig. 10a). The cumulative AE's at C′ are always <20 in number. Indeed, during crack closure and compactant deformation (e.g with negative porosity changes), the samples accommodate deformation in a purely elastic manner, therefore no radiated energy (i.e AE) is expected from microcrack nucleation or propagation while porosity decreases with increasing deformation. The increase in AE's between yield and peak stress suggests that most of the crack propagation occurs only after the yield stress is passed and not when the onset of dilatancy is passed. In terms of porosity change, it follows this time a concave downward shape (inverse "U-type") at intermediate foliation orientations ($\beta = 30$,45, and 60°), contrary to the mechanical properties and acoustic emissions. It was observed (Fig. 10b, dark grey circles) that total porosity change was ~0 at yield stress. In other words, at yield stress, the newly created porosity due to nucleation and propagation of micro cracks nearly compensated micro crack closure by differential stress. The concave-downward shape of the porosity change at intermediate β (30, 45 and 60°) can be qualitatively predicted by the volume change in one single wing-crack oriented at β. In fact, the opening volume (V_{wing}) of 3-D wing cracks growing in compression has a dependency on the orientation of the crack towards the major principal stress as[12]:

$$V_{wing} = 3(1-\nu)\sigma^3.a^4.\left(2E\left(1-\nu^2\right)K_{1c}^2\right).\left((\sin\beta)^2.\cos\beta.(1-\tan\beta.\tan\varphi)\right)^3$$

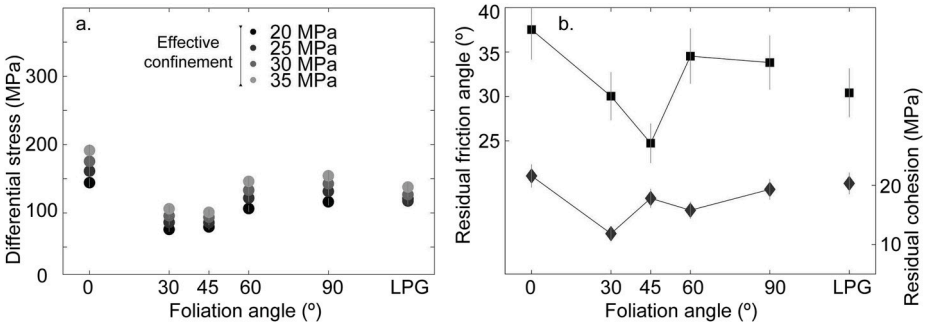

Fig. 9. Residual strength of failed samples function of the foliation angle. **a**. Values of residual differential stress with increasing confining pressures. **b**. Calculated residual friction angle (left y-axis, squares) and residual cohesion (right y-axis, diamonds).

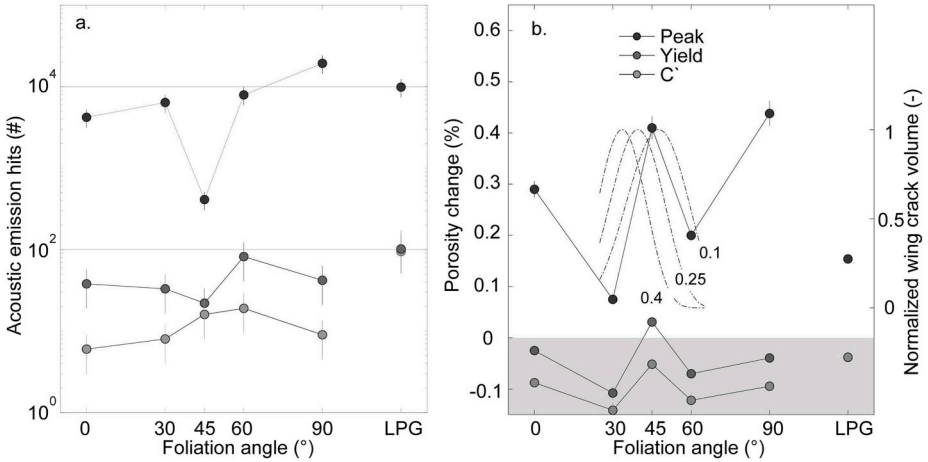

Fig. 10. Acoustic Emissions and porosity changes at different stages of triaxial deformation. **a.** Cumulative number of acoustic Emissions recorded at onset of dilatancy, yield stress and peak strength. **b.** right y-axis shows total porosity change measured at onset of dilatancy, yield stress and peak strength (negative porosity change reflects overall compaction (grey area) and positive reflects overall dilation). Left y-axis shows normalized 3-D wing crack volume function of their orientation[12] for different internal friction values.

with ν the sample's Poisson's ratio, σ the applied stress on the sliding crack, a the sliding crack's half length, E its Young's modulus, K_{1c} its fracture toughness, and φ its internal friction angle (note that in Dyskin et al.,[12] the orientation towards the major principal stress is called α and the internal friction angle is called μ). Normalizing the expression of the wing crack volume by $3(1-\nu)\sigma^3.a^4.(2E(1-\nu^2)K_{1c}^2)$ (e.g by the amount of deformation) shows that the normalized volume of the wing crack's dependence on β (Fig. 10b, right y-axis) has a similar concave-downward shape for intermediate angles. This qualitatively predicts our experimental observations, showing an "inversed U-shaped" behavior at intermediate foliation angles, and confirms that the porosity change in *CGn* is due to the nucleation and propagation of wing cracks as is the case for isotropic crystalline rocks.[9,22] Note that for angles 0 and 90°, the deformation processes related to crack initiation and propagation are slightly different (biotite kinking and faulting instead of wing crack propagation (see section 4.1 and Ref.[15]) therefore no attempt is made to predict the porosity change at those angles.

Based on the previous observation, it is safe to assume that most of the volumetric change at $\beta = 45°$ is due to the Mode I opening of wing cracks. It is therefore not surprising that the total number of AE's recorded at the yield and peak stresses is lower in that experiment than in experiments at other β. In fact, Mode I crack nucleation and propagation is expected to generate no (or very few) AE's while Modes II and III fracture propagation are associated to high AE rates.[73]

5.2. Apparent permeability of intact and failed transverse isotropic rock

Apparent permeability of intact samples decreased with increasing $\sigma_1' = \sigma_3'$ for all foliation angles (Fig. 4g-l). The decrease of permeability with isostatic confinement is due to closure of the micro crack network as well as to closure of the contacts between foliation layers. The latter reduces the matrix and interlayer volume and the rock's capacity to transport fluid[32,33] and therefore its permeability.

Apparent permeability decreased with increasing foliation angle (β) at all stresses (Fig. 5b). This observation reflects primarily the tortuosity of the hydraulic path.[17,18,27–30,43] At orientations of 0°, the preferential fluid paths (parallel to the biotite layers) are oriented in the sense of fluid flow, allowing large flow rates. At orientations of 90°, the preferential fluid paths are perpendicular to the flow. In this case, the foliation acts as a barrier rather than as preferential fluid path.[30] It is noticeable that permeability at $\beta = 90°$ were the lowest but still ~4 times higher than those of intact isotropic granite.

Apparent permeabilities of *CGn* measured under failed-residual conditions (Fig. 5b, grey triangles) were usually larger than those measured under intact-isostatic conditions due to the formation of fractures. At $\beta = 0°$, apparent permeability did not drop after reduction of the differential stress because the newly formed sub-vertical fractures were not closed. Indeed the normal stress $\sigma_N = \frac{1}{2}[(\sigma_1+\sigma_3)-(\sigma_1-\sigma_3)cos(2\theta)]$calculated on the fractures (oriented at θ towards the vertical, Fig. 6b) remained low at $\beta = 0°$ (σ_N~40 MPa). At $\beta = 30°$, permeability did not increase after failure. In fact, at this orientation, the main fracture followed very closely the foliation and did not create any connection between different mineral layers (Fig. 6) suggesting that, because the differential stress remained high ($\sigma_N \sim 70$ MPa), the new fracture remained closed. This is further supported by the increase in permeability of ~3 times after the decrease in differential stress. At all other orientations the fractures showed "en-echelon structures", creating connections between the mineral layers, increasing permeability after faulting.

Many studies dealing with the permeability of anisotropic rocks have measured it in one or two directions, manly perpendicular and parallel

to the main foliation[47,50,74] direction. Most numerical models have thus relied on theoretical analyses of the full permeability tensor[45,51] to extrapolate rock permeability to two or three dimensions. In theory, the permeability tensor for transverse isotropic rock as function of the angle to the fluid flow (here β) can be simplified in two dimensions as[45,51,56]:

$$k(\beta) = k_{0^\circ}.\cos^2\beta + k_{90^\circ}.\sin^2\beta$$

where k_{0° and k_{90° are the apparent permeabilities at 0 and 90° (necessarily the maximum and minimum permeabilities respectively). Comparison of our results with the permeability tensor (Fig. 11a) shows that the theoretical prediction is valid within less than a factor 2 error for the intact samples under isostatic stress (black circles). Nevertheless, when considering the failed samples, we observe that the prediction fails at all intermediate foliations (grey circles and triangles in Fig. 11a) with more than an order of magnitude difference. This large difference arises from the very different failure structure at $\beta = 0^\circ$ which strongly enhances fluid flow with respect to all other experiments. In fact, modifying the permeability tensor to:

$$k(\beta) = k_{30^\circ}.\cos^2\beta + k_{90^\circ}.\sin^2\beta$$

taking k_{30° as the maximum apparent permeability yields a much better prediction to the experimental permeability in failed samples (Fig. 11b). This result demonstrates that measurements of parallel and perpendicular permeability are not sufficient for the estimation of the full permeability tensor in fractured rock. This is especially valid when the fracture structure depends on the foliation angle. In fact, our results suggest that the estimation of permeability in transverse isotropic rock is highly sensitive to i) fracture structure (direction with respect to flow, geometry and roughness) ii) fracture connectivity (e.g experiment at 90°), iii) stress applied on the fractures[75] and therefore the orientation of the stress field.

5.3. P-wave velocity of intact and failed transverse isotropic rock

During isostatic confinement, for each foliation orientation, P-wave velocities increased with increasing $\sigma_1' = \sigma_3'$ (Fig. 5a–f). Such behavior has been observed in igneous,[41,42] sedimentary,[76,77] and metamorphic rocks.[78] Increase in V_p is due to closure of the micro cracks present in the rock with increasing pressure. At stresses >50 MPa, compressional velocity is expected to reach a maximum in particular in igneous[41] and metamorphic rocks[78] as cracks become fully closed. In this study, the experiments were performed under stresses representative of underground reservoirs (σ_3'= 20 MPa), we expect that cracks are not fully closed when deformation started. With regards to foliation angle, V_p decreased with increasing β at all confinements (Fig. 2). Such effect is expected since V_p is highly dependent on the orientation and length of foliation structures in the rock.[78,79] In addition, 90° samples are expected to have higher axial compressibility than 0° samples due to layering of stiff minerals (Quartz, Feldspar) with compliant ones (Biotite),[79] thus lower compressional velocities.[30,81]

The observation that V_p was usually lower under failed-residual conditions (Fig. 5a, grey triangles) than under intact-isostatic conditions (Fig. 5a, black circles) indicates that the presence of the macroscopic fracture and its structure towards the wave path excerts a control on the velocity field. Nevertheless, the fact that V_p were largest under failed-residual conditions (e.g when differential stress was still high) than under failed-isostatic conditions (Fig. 5a) suggests that the major control of V_p is not only the presence of macroscopic fractures but the stress acting on them.[7]

6. Discussion and implications for Enhanced Geothermal Systems

Two types of properties based on the response to foliation angle can be distinguished from our study. The first group of properties are those that follow a "U-type" of anisotropy. In this group, we can classify all the mechanical properties in terms of stress (at C′, and yield stress) and strength (peak and residual strength). Here can be included also the changes in porosity during deformation (at intermediate foliation angles) with an "inversed U-shape". The "U-type" anisotropy of these properties with increasing foliation angle is due to the fact that all of them are 'friction' controlled. To rephrase, the mechanical properties are controlled by the frictional response of weak planes (biotite layers or grains) and therefore depend on the deformation mode of the weakest elements. As shown in sections 4 and 5, such properties can be accurately predicted by anisotropic wing crack models. The second group are the properties that follow a "decreasing order shape"[67] with increasing foliation angle. In this group, we can classify the apparent permeability and P-wave velocity. These properties are instead controlled by the changes in microstructure of the whole sample volume. It is important to distinguish between these two types of properties because usually, geophysical exploration of EGS and other Geo-energy activities relies on the use of surface measurements (seismic reflection and refraction) as well as borehole measurements (wellbore seismics and injectivity logs).[82]

On the one hand, surface and wellbore seismics rely on the propagation of seismic waves to determine the reservoir properties. As shown in Sections 3 and 5 of this study, wave propagation across anisotropic crystalline rocks is highly dependent on i) the direction of propagation with respect to the main foliation, ii) the rock's stress state, and iii) the damage state of the reservoir. As an example, one can observe from Fig. 4a, that V_p ~5591 m s^{-1} at $\beta = 0^\circ$ under 5 MPa effective isostatic confinement. Nevertheless, the P-wave velocity is also equal to 5606 m s^{-1} at $\beta = 90^\circ$ under 25 MPa confinement at the residual stress with the presence of a macroscopic fracture. In addition, during EGS stimulation and operation phases, monitoring of induced seismicity requires a good knowledge of the velocity field in the reservoir which can be delicate to establish.[83–87] In transverse isotropic crystalline rocks, V_p shows an almost monotonic decrease with increasing foliation angle (Fig. 2a–f and

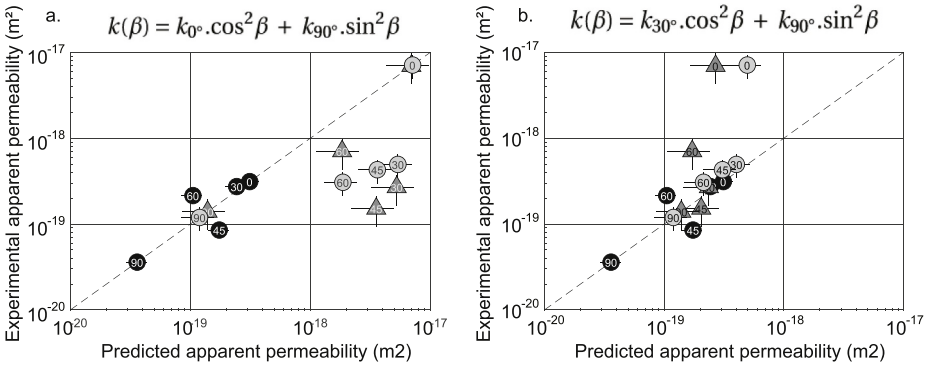

Fig. 11. Comparison of experimental and theoretical apparent permeability. **a.** Experimental versus theoretically predicted apparent permeability through $k_\beta = k_{0^\circ}.\cos^2\beta + k_{90^\circ}.\sin^2\beta$ where k_{0° is the permeability of the sample with foliation orientation parallel to fluid flow. **b.** same graph as a. this time theoretical estimation is done through $k_\beta = k_{30^\circ}.\cos^2\beta + k_{90^\circ}.\sin^2\beta$ where k_{30° is the permeability of the sample with foliation oriented at 30° towards fluid flow. Black circles correspond to measurements of intact samples under isotropic stress state ($\sigma_1' = \sigma_3'$=20 MPa). Grey triangles correspond to failed samples at residual stress state ($\sigma_1' >> \sigma_3'$). Grey circles correspond to measurements of failed samples under isotropic stress state ($\sigma_1' = \sigma_3'$=20 MPa).

Fig. 5a) but an increase with isotropic confinement and deviatoric stress. In addition, the presence of a fracture does not necessarily result in a sharp decrease of P-wave velocity if the differential stress on the fault is high (Fig. 5a). Such effects could compensate each other and add further difficulties to the characterization of the reservoir's velocity structure. The measurements provided in this study and especially the shape of the velocity profile with respect to foliation angle can be used as reference for estimation of the anisotropic velocity structure of the reservoir if the local stress field is known.

On the other hand, wellbore injectivity measurements rely on fluid percolation through a rock mass which can be highly anisotropic and damaged. In the light of our results, reservoirs whose foliation is oriented at 45° towards the major principal stress (or the largest stress change) could present i) higher increases in porosity with respect to reservoirs with other foliation orientations as a response to external forcing and ii) lower seismicity related to high increases in porosity due to preferential Mode I fracture development. Note nevertheless that these results are valid for intact rock and not for faults where the mechanics and hydraulic transport properties are rather controlled by the fracture, thus the permeability tensor must be used with care when estimating reservoir hydraulic transport properties. Speculation on the apparent permeability results of intact and faulted rock (Figs. 2 and 5) implies that fluid injections in lightly fractured (or intact) gneissic reservoir rocks are highly dependent on the direction of the injection well with respect to the reservoir's foliation and also towards the stress field. Rock foliation is expected to contribute to permeability anisotropy due to i) preferential formation of faults along foliation planes ii) permeability reduction for un-sheared optimally oriented faults (e.g case of 30°). iii) Increase in permeability by fracture connectivity if failure planes are not optimally oriented (e.g $\beta = 45, 60, 90°$) (for example by the formation of en-echelon fractures). In this case the reservoir's volume is expected to largely increase compared to the 0° and 30° case. Such results should be taken in account in addition to the anisotropic permeability resulting from stress.[7] Finally, the hydro-mechanical coupling between anisotropic rock fractures and geo-fluids should be taken into account. In fact, the strength of the continental crust, which is largely composed of igneous (e.g. granitic composition, isotropic and non-isotropic) and metamorphic rocks, is mostly controlled by the strength of fractures present in the rock.[7,70] In turn, the formation of fractures and their mechanical properties are controlled by preferential orientation of minerals and foliation present in the initially undeformed rock.[15,63–65] The combined use of damage initiation (section 4.1), intact rock failure (section 4.2, for details on many different anisotropic failure criteria, refer to Ref. [6,18,63–65,89–92] and residual friction (Section 4.3) can be readily used as inputs for reservoir models as long as the scale dependence of rock failure is taken into account.[7,64] Nevertheless, geological characterization of the fractures in the reservoir (i.e if the fracture planes follow the foliation or if they present "en-echelon" structures) is needed. A good knowledge of the reservoirs' anisotropic structure is of outmost importance to estimate reservoir integrity, hydraulic transport through it, and the related seismic hazard.

Several studies have demonstrated close links between the rock microstructure and its hydraulic transport capacity.[28,47,49,74,93] In crystalline rocks,[74] the main control on fluid flow anisotropy is the creation of porous structures due to shear induced cataclasis. In foliated rocks, we can conclude that well before the occurrence of cataclasis, porosity can be created due to damage initiation on preferentially oriented microcracks (e.g dilation at $\beta = 45°$), inducing fluid flow anisotropy. In turn, preferentially oriented porosity changes in geo-energy reservoirs can highly affect i) directional permeability, thus affecting the injection-extraction capacity of the reservoir and ii) it can generate oriented stress changes modifying induced seismicity rates.[94] A comprehensive analysis of foliation orientation towards tectonic regime and wellbore orientation is needed to further assess this issue. In terms of induced seismicity in geo-energy reservoirs, there is an ongoing debate on the shape of the seismicity clouds triggered by anthropogenic activity.[83–87] In fact, during reservoir stimulation, the seismicity clouds can be oriented either towards the major principal stress (in Basel EGS stimulation[95]; in the Aspo Hard Rock Laboratory, Sweden[86]; in the Helsinki EGS stimulation, Finland (Kwiatek et al., 2019)) or towards the optimal fault orientation (e.g ~30+-5° to the major principal stress) For example, in the Cooper Basin stimulation[96]; and deep well injection in Youngstown, Ohio.[85] We can speculate that the observed patterns of fracture formation in anisotropic crystalline rock can be related to both these situations. On the one hand, if the foliation angle is low with respect to the major principal stress, the fracture formation will be oriented in the sense of $\boldsymbol{\sigma}_1$. The fracture network as well as the interlayer pore space are preferential conduits for fluid, thus the seismicity cloud would grow in the sense of the major principal stress. Then, at intermediate angles (~30°), the fractures are expected to form in angles close to optimally oriented towards the stress field. There, the seismicity cloud should propagate approximately towards the optimally oriented direction. Finally, at higher angles (45–90°), the formation of en-echelon fractures can lead to a combination of both processes and generate branching in the propagation of seismicity clouds, potentially as observed during the Basel geothermal stimulation.[84a,95] Nevertheless, to confirm this analysis further work is needed.

7. Conclusions

The design and implementation of geo-energy reservoirs requires appropriate knowledge and control of the mechanical and hydraulic transport properties of the host rock which is usually anisotropic in the case of EGS in central Europe. From our experiments conducted under geo-energy reservoir conditions, the main observations are as follows:

The mechanical properties of transverse isotropic gneiss (onset of dilatancy, peak strength, and residual failure envelope) follow a "U-shaped" anisotropy with respect to foliation orientation with maxima at 0 and 90° and minima at 30° towards the major principal stress. These properties can be explained by anisotropic wing crack models dominated by the foliation orientation.

The porosity increase during stress induced damage is highly dependent on foliation orientation and is largest at 45° towards the major principal stress, following an "inverse U-shape" at intermediate foliation angles. This behaviour is due to large volumetric changes associated with tensile opening of anisotropic wing cracks and can thus be predicted by analytical models.

The total number of Acoustic Emissions during deformation also depends on foliation orientation, being minimum at 45°. This observation is compatible with the majority of damage generated in tensile mode (rather than shear modes) by the propagation of anisotropic wing cracks at this angle.

Apparent permeability is the largest when the foliation is parallel to the fluid flow and progressively decreases with increasing angle of foliation to fluid flow. Changes in permeability in fractured rock cannot be estimated through the permeability tensor relying solely on measurements parallel and perpendicular to the main foliation. In fact, permeability is highly dependent on i) the orientation of the fracture with respect to fluid flow, ii) the fracture structure (e.g "en-echelon" structures are more permeable), and iii) on the stress acting on the fractures.

P-wave velocity is largest when the foliation is parallel to the wave propagation direction and progressively decreases with increasing angle of foliation. Changes in P-wave velocity (e.g. increase, due to differential stress, and decrease due to fracturing) are of similar magnitude at all foliation angles.

Such results will help design and implement geo-energy reservoirs hosted in transverse isotropic granitic formations in particular in central Europe.

Data availability

All the data related to this manuscript can be found on Zenodo.org under repository number 3627047.

Declaration of competing interest

The authors declare no competing interests.

Acknowledgments

M.A. and M.V. acknowledge the funding support from the Swiss National Science Foundation (SNF), project no. PYAPP2160588, and the technical staff at LEMR for help with sample preparation. M.V. acknowledges the European Research Council Starting Grant project 757290-BEFINE. M.A acknowledges Barnaby Fryer; for fruitful discussions. The authors thank two anonymous reviewers for pertinent comments that improved the manuscript.

Appendix A. Supplementary data

Supplementary data to this article can be found online at https://doi.org/10.1016/j.ijrmms.2020.104235.

Annex 1. Experimental tables

Table A1
Mechanical data from the conducted experiments.

	Imposed stress conditions			Stress values				Acoustic Emissions			Porosity Change		
Foliation angle	Radial Stress	Fluid Pressure	Intact/ Failed	Onset of dilatancy C′	Yield stress	Peak Stress	Residual Stress	AE # at C′	AE # at yield stress	AE at peak stress	Porosity at C′	Porosity at yield stress	Porosity at peak stress
◦	MPa	MPa	I/F	MPa	MPa	MPa	MPa	#	#	#	–	–	–
0	25	5	I	159.8	221.3	290.4	–	6	38	4206	– 0.000877	– 0.00025	0.0029
0	25	5	F	–	–	–	144.4	–	–	–	–	–	–
0	30	5	F	–	–	–	161.4	–	–	–	–	–	–
0	35	5	F	–	–	–	175.6	–	–	–	–	–	–
0	40	5	F	–	–	–	191.6	–	–	–	–	–	–
30	25	5	I	118.2	128.3	172.6	–	8	33	6393	– 0.001415	– 0.001079	0.00075
30	25	5	F	–	–	–	76.01	–	–	–	–	–	–
30	30	5	F	–	–	–	86.31	–	–	–	–	–	–
30	35	5	F	–	–	–	95.91	–	–	–	–	–	–
30	40	5	F	–	–	–	106.2	–	–	–	–	–	–
45	25	5	I	76.42	106.4	145.6	–	16	22	411	– 0.000516	0.0003083	0.0041
45	25	5	F	–	–	–	79.61	–	–	–	–	–	–
45	30	5	F	–	–	–	86.09	–	–	–	–	–	–
45	35	5	F	–	–	–	93.85	–	–	–	–	–	–
45	40	5	F	–	–	–	101	–	–	–	–	–	–
60	25	5	I	117.8	160.6	199.5	–	19	82	7921	– 0.001221	– 0.0007021	0.002
60	25	5	F	–	–	–	106.5	–	–	–	–	–	–
60	30	5	F	–	–	–	121.9	–	–	–	–	–	–
60	35	5	F	–	–	–	133.4	–	–	–	–	–	–
60	40	5	F	–	–	–	146.3	–	–	–	–	–	–
90	25	5	I	139.4	197.8	265	–	9	42	19330	– 0.0009454	– 0.0003944	0.00438
90	25	5	F	–	–	–	116.4	–	–	–	–	–	–
90	30	5	F	–	–	–	131.7	–	–	–	–	–	–
90	35	5	F	–	–	–	142.9	–	–	–	–	–	–
90	40	5	F	–	–	–	154.5	–	–	–	–	–	–
LPG	25	5	I	245.9	242.7	308.4	–	102	114	9873	– 0.0003793	– 0.0003817	0.00154
LPG	25	5	F	–	–	–	120.7	–	–	–	–	–	–
LPG	30	5	F	–	–	–	117.5	–	–	–	–	–	–
LPG	35	5	F	–	–	–	126.9	–	–	–	–	–	–
LPG	40	5	F	–	–	–	138	–	–	–	–	–	–

Table A2
P-wave velocities and apparent permeability from the condcuted experiments

Foliation angle	Axial Stress	Radial Stress	Fluid Pressure	Effective Radial Stress	Intact/Failed	V_p	k_{app}
◦	MPa	MPa	MPa	MPa	I/F	m/s	m^2
0	1	1	0	1	I	5464.20	
0	5	5	0	5	I	5557.81	

(continued on next page)

Table A2 (*continued*)

Foliation angle	Axial Stress	Radial Stress	Fluid Pressure	Effective Radial Stress	Intact/Failed	V_p	k_{app}
∘	MPa	MPa	MPa	MPa	I/F	m/s	m^2
0	5	5	1	4	I	5569.92	
0	10	10	1	9	I	5622.30	
0	10	10	5	5	I	5587.46	2.49E-19
0	10	10	5	5	I	5591.54	
0	15	15	5	10	I	5645.54	4.94E-19
0	15	15	5	10	I	5662.23	
0	25	25	5	20	I	5760.21	3.12E-19
0	25	25	5	20	I	5762.38	
0	165	25	5	20	F	5857.02	6.93E-18
0	167	25	5	20	F	5863.79	
0	167	25	5	20	F	5872.84	
30	1	1	0	1	I	5281.31	
30	5	5	0	5	I	5420.71	
30	5	5	1	4	I	5420.71	
30	10	10	1	9	I	5505.80	
30	10	10	5	5	I	5462.47	1.96E-19
30	10	10	5	5	I	5451.18	
30	10	10	5	5	I	5446.67	
30	15	15	5	10	I	5571.43	3.77E-19
30	25	25	5	20	I	5638.17	2.73E-19
30	25	25	5	20	I	5626.13	
30	98	25	5	20	F	5771.55	2.69E-19
30	100	25	5	20	F	5771.55	
30	103	25	5	20	F	5571.94	
30	25	25	5	20	F	5533.18	4.94E-19
30	25	25	5	20	F	5537.87	
30	25	25	5	20	F	5542.56	
30	25	25	5	20	F	5549.62	
45	5	5	0	5	I	5182.51	
45	5	5	1	4	I	5220.55	
45	5	5	1	4	I	5246.22	
45	10	10	1	9	I	5339.20	
45	10	10	1	9	I	5343.02	
45	10	10	5	5	I	5323.97	1.08E-19
45	10	10	5	5	I	5318.28	
45	10	10	5	5	I	5316.38	
45	15	15	5	10	I	5360.63	1.02E-19
45	15	15	5	10	I	5391.62	
45	15	15	5	10	I	5387.73	
45	20	20	5	15	I	5441.72	1.51E-19
45	20	20	5	15	I	5465.64	
45	25	25	5	20	I	5494.81	5.17E-20
45	25	25	5	20	I	5517.16	
45	25	25	5	20	I	5517.16	
45	105	25	5	20	F	5657.48	6.55E-19
45	105	25	5	20	F	5659.65	
45	100	25	5	20	F	5651.00	
45	96	25	5	20	F	5653.16	
45	25	25	5	20	F	5430.17	1.10E-18
45	25	25	5	20	F	5412.33	
45	25	25	5	20	F	5412.33	
60	1	1	0	1	I	5207.37	
60	5	5	0	5	I	5289.11	
60	5	5	1	4	I	5305.68	
60	10	10	1	9	I	5342.43	
60	10	10	5	5	I	5315.18	1.50E-19
60	10	10	5	5	I	5313.10	
60	15	15	5	10	I	5344.91	3.13E-19
60	15	15	5	10	I	5383.15	
60	20	20	5	15	I	5477.83	1.71E-19
60	25	25	5	20	I	5470.06	2.14E-19
60	25	25	5	20	I	5474.48	
60	136	25	5	20	F	5665.29	7.04E-19
60	131	25	5	20	F	5658.11	
60	131	25	5	20	F	5665.29	
60	25	25	5	20	F	5373.77	3.06E-19
60	25	25	5	20	F	5378.07	
60	25	25	5	20	F	5358.76	
90	1	1	0	1	I	4910.32	
90	5	5	0	5	I	5153.40	
90	5	5	1	4	I	5151.66	
90	5	5	1	4	I	5153.40	
90	10	10	1	9	I	5225.15	
90	10	10	1	9	I	5223.35	

(*continued on next page*)

Table A2 (*continued*)

Foliation angle	Axial Stress	Radial Stress	Fluid Pressure	Effective Radial Stress	Intact/Failed	V_p	k_{app}
°	MPa	MPa	MPa	MPa	I/F	m/s	m^2
90	10	10	5	5	I	5217.98	5.77E-20
90	10	10	5	5	I	5219.77	
90	10	10	5	5	I	5225.15	
90	15	15	5	10	I	5256.14	4.99E-20
90	15	15	5	10	I	5279.86	
90	15	15	5	10	I	5283.53	
90	20	20	5	15	I	5332.59	4.99E-20
90	20	20	5	15	I	5349.47	
90	20	20	5	15	I	5353.24	
90	25	25	5	20	I	5373.06	3.60E-20
90	25	25	5	20	I	5403.63	
90	139	25	5	20	F	5591.86	1.39E-19
90	142	25	5	20	F	5585.62	
90	143	25	5	20	F	5593.95	
90	144	25	5	20	F	5585.62	
90	147	25	5	20	F	5606.48	
90	25	25	5	20	F	5312.07	1.19E-19
90	25	25	5	20	F	5332.75	
90	25	25	5	20	F	5317.69	
LPG	1	1	0	1	I	5687.25	
LPG	5	5	0	5	I	5710.83	
LPG	5	5	1	4	I	5658.91	
LPG	5	5	1	4	I	5667.15	
LPG	10	10	1	9	I	5701.76	
LPG	10	10	5	5	I	5683.01	
LPG	10	10	5	5	I	5695.50	6.03E-20
LPG	15	15	5	10	I	5725.33	
LPG	15	15	5	10	I	5735.89	1.17E-20
LPG	20	20	5	15	I	5758.22	
LPG	20	20	5	15	I	5771.05	
LPG	25	25	5	20	I	5776.44	1.31E-20
LPG	25	25	5	20	I	5791.51	1.30E-20
LPG	148	25	5	20	F	5701.88	8.86E-20
LPG	123	25	5	20	F	5620.45	
LPG	25	25	5	20	F	5611.46	
LPG	25	25	5	20	F	5607.37	1.86E-20

References

1 Zang A, Oye V, Jousset P, et al. Analysis of induced seismicity in geothermal reservoirs–An overview. *Geothermics*. 2014;52:6–21.
2 Wehrens P, Berger A, Peters M, Spillmann T, Herwegh M. Deformation at the frictional-viscous transition: evidence for cycles of fluid-assisted embrittlement and ductile deformation in the granitoid crust. *Tectonophysics*. 2016;693:66–84.
3 Wehrens P, Baumberger R, Berger A, Herwegh M. How is strain localized in a meta-granitoid, mid-crustal basement section? Spatial distribution of deformation in the central Aar massif (Switzerland). *J Struct Geol*. 2017;94:47–67.
4 Amann F, Gischig V, Evans K, et al. The seismo-hydromechanical behavior during deep geothermal reservoir stimulations: open questions tackled in a decameter-scale in situ stimulation experiment. *Solid Earth*. 2018;9(1):115–137.
5 Wenning QC, Madonna C, de Haller A, Burg JP. Permeability and seismic velocity anisotropy across a ductile-brittle fault zone in crystalline rock. *Solid Earth*. 2018;9(3):683–698.
6 Jaeger JC. Shear failure of anisotropic rocks. *Geol Mag*. 1960;97:65–72.
7 Zoback MD. *Reservoir Geomechanics*. Cambridge University Press; 2010.
8 Brace WF, Bombolakis EG. A note on brittle crack growth in compression. *J Geophys Res*. 1963;68(12):3709–3713.
9 Brace WF, Paulding Jr BW, Scholz CH. Dilatancy in the fracture of crystalline rocks. *J Geophys Res*. 1966;71(16):3939–3953.
10 Sammis CG, Ashby MF. The failure of brittle porous solids under compressive stress states. *Acta Metall*. 1986;34(3):511–526.
11 Ashby MF, Sammis CG. The damage mechanics of brittle solids in compression. *Pure Appl Geophys*. 1990;133(3):489–521.
12 Dyskin AV, Germanovich LN, Ustinov KB. A 3-D model of wing crack growth and interaction. *Eng Fract Mech*. 1999;63(1):81–110.
13 Paterson MS, Wong TF. *Experimental Rock Deformation-The Brittle Field*. Springer Science & Business Media; 2005.
14 Martin CD, Chandler NA. The progressive fracture of Lac du Bonnet granite. *Int J Rock Mech Min Sci Geomech Abstr*. 1994;31(6):643–659.
15 Rawling GC, Baud P, Wong TF. Dilatancy, brittle strength, and anisotropy of foliated rocks: experimental deformation and micromechanical modeling. *J Geophys Res: Solid Earth*. 2002;107(B10). ETG-8.
16 Guéguen Y, Palciauskas V. *Introduction to the Physics of Rocks*. Princeton University Press; 1994.
17 Paterson MS. The equivalent channel model for permeability and resistivity in fluid-saturated rock—a re-appraisal. *Mech Mater*. 1983;2(4):345–352.
18 Walsh JB, Brace WF. The effect of pressure on porosity and the transport properties of rock. *J Geophys Res: Solid Earth*. 1984;89(B11):9425–9431.
19 Tapponnier P, Brace WF. Development of stress-induced microcracks in Westerly granite. *Int. J. Rock Mech. Min. Sci. Geomech. Abstr*. 1976;13(4):103–112. Pergamon.
20 Wong TF. Micromechanics of faulting in Westerly granite. *Int J Rock Mech Min Sci Geomech Abstr*. 1982;19(No. 2):49–64 (Pergamon).
21 Lockner DA. A generalized law for brittle deformation of Westerly granite. *J Geophys Res: Solid Earth*. 1998;103(B3):5107–5123.
22 Zoback MD, Byerlee JD. The effect of microcrack dilatancy on the permeability of Westerly granite. *J Geophys Res*. 1975;80(5):752–755.
23 Violay M, Gibert B, Mainprice D, Burg JP. Brittle versus ductile deformation as the main control of the deep fluid circulation in oceanic crust. *Geophys Res Lett*. 2015;42(8):2767–2773.
24 Violay M, Heap MJ, Acosta M, Madonna C. Porosity evolution at the brittle-ductile transition in the continental crust: implications for deep hydro-geothermal circulation. *Sci Rep*. 2017;7(1):7705.
25 Caine JS, Evans JP, Forster CB. Fault zone architecture and permeability structure. *Geology*. 1996;24(11):1025–1028.
26 Faulkner DR, Jackson CAL, Lunn RJ, et al. A review of recent developments concerning the structure, mechanics and fluid flow properties of fault zones. *J Struct Geol*. 2010;32(11):1557–1575.
27 Huenges E, Erzinger J, Kück J, Engeser B, Kessels W. The permeable crust: geohydraulic properties down to 9101 m depth. *J Geophys Res: Solid Earth*. 1997;102(B8):18255–18265.
28 Faulkner DR, Rutter EH. Comparisons of water and argon permeability in natural clay-bearing fault gouge under high pressure at 20° C. *J Geophys Res: Solid Earth*. 2000;105(B7):16415–16426.
29 Arch J, Maltman A. Anisotropic permeability and tortuosity in deformed wet sediments. *J Geophys Res: Solid Earth*. 1990;95(B6):9035–9045.
30 Kawano S, Katayama I, Okazaki K. Permeability anisotropy of serpentinite and fluid pathways in a subduction zone. *Geology*. 2011;(10):939–942, 201; 1 39.
31 Reches ZE, Lockner DA. Nucleation and growth of faults in brittle rocks. *J Geophys Res: Solid Earth*. 1994;99(B9):18159–18173.
32 Mitchell TM, Faulkner DR. Experimental measurements of permeability evolution during triaxial compression of initially intact crystalline rocks and implications for fluid flow in fault zones. *J Geophys Res: Solid Earth*. 2008;113(B11).
33 Brace W, Walsh JB, Frangos WT. Permeability of granite under high pressure. *J Geophys Res*. 1968;73(6):2225–2236.

34 Kranz RL, Frankel AD, Engelder T, Scholz CH. The permeability of whole and jointed Barre granite. *Int. J. Rock Mech. Min. Sci. Geomech. Abstr.* 1979;vol. 16(4):225–234. Pergamon.
35 Summers R, Winkler K, Byerlee J. Permeability changes during the flow of water through Westerly Granite at temperatures of 100–400 C. *J Geophys Res: Solid Earth.* 1978;83(B1):339–344.
36 Heard HC, Page L. Elastic moduli, thermal expansion, and inferred permeability of two granites to 350 C and 55 megapascals. *J Geophys Res: Solid Earth*. 1982;87(B11): 9340–9348.
37 Bernabé Y. The effective pressure law for permeability in Chelmsford granite and Barre granite. *Int. J. Rock Mech. Min. Sci. Geomech. Abstr.* 1986;vol. 23(3):267–275. Pergamon.
38 Teufel LW. *Permeability Changes during Shear Deformation of Fractured Rock (No. SAND-86-2522C; CONF-870625-4)*. Albuquerque, NM (USA): Sandia National Labs.; 1987.
39 Moore DE, Lockner DA, Byerlee JD. Reduction of permeability in granite at elevated temperatures. *Science*. 1994;265(5178):1558–1561.
40 Darot M, Reuschlé T. Acoustic wave velocity and permeability evolution during pressure cycles on a thermally cracked granite. *Int J Rock Mech Min Sci*. 2000;37(7): 1019–1026.
41 Nasseri MHB, Schubnel A, Benson PM, Young RP. Common evolution of mechanical and transport properties in thermally cracked westerly granite at elevated hydrostatic pressure. *Pure Appl Geophys*. 2009;166(5-7):927–948.
42 Wang XQ, Schubnel A, Fortin J, Guéguen Y, Ge HK. Physical properties and brittle strength of thermally cracked granite under confinement. *J Geophys Res: Solid Earth.* 2013;118(12):6099–6112.
43 Brace WF. October. Permeability of crystalline and argillaceous rocks. *Int. J. Rock Mech. Min. Sci. Geomech. Abstr.* 1980;vol. 17(5):241–251. Pergamon.
44 Nover G, Will G. Laboratory measurements on KTB core samples: complex resistivity, zeta potential, permeability, and density as a tool for the detection of flow phenomena. *Sci Drill.* 1991;2:90–100.
45 Bernabé Y. On the measurement of permeability in anisotropic rocks. *Int. Geophys.* 1992;vol. 51:147–167. Academic Press.
46 Clauser C. Permeability of crystalline rocks. *Eos, Trans. Am. Geophys. Union*. 1992;73 (21):233–238.
47 Morrow C, Lockner D, Hickman S, Rusanov M, Röckel T. Effects of lithology and depth on the permeability of core samples from the Kola and KTB drill holes. *J Geophys Res: Solid Earth.* 1994;99(B4):7263–7274.
48 Rasolofosaon PN, Zinszner BE. Comparison between permeability anisotropy and elasticity anisotropy of reservoir rocks. *Geophysics*. 2002;67(1):230–240.
49 Wibberley CA, Shimamoto T. Internal structure and permeability of major strike-slip fault zones: the median tectonic line in mie prefecture, southwest Japan. *J Struct Geol.* 2003;25(1):59–78.
50 Orellana Espinoza LF. *Frictional and Transport Properties of Faults Zones in the Opalinus Clay Formation Doctoral Dissertation*. EPFL; 2018.
51 Renard P, Genty A, Stauffer F. Laboratory determination of the full permeability tensor. *J Geophys Res: Solid Earth.* 2001;106(B11):26443–26452.
52 Casasopra S. *Studio petrografico dello gneiss granitico Leventina: Valle Riviera e Valle Leventina (Canton Ticino)*. Doctoral dissertation. ETH Zurich; 1940.
53 Darot M, Gueguen Y, Baratin ML. Permeability of thermally cracked granite. *Geophys Res Lett*. 1992;19(9):869–872.
54 David C, Menéndez B, Darot M. Influence of stress-induced and thermal cracking on physical properties and microstructure of La Peyratte granite. *Int J Rock Mech Min Sci*. 1999;36(4):433–448.
55 Noël C, Pimienta L, Violay M. Time-dependent deformations of sandstone during pore fluid pressure oscillations: implications for natural and induced seismicity. *J Geophys Res: Solid Earth.* 2019;124(1):801–821.
56 Zhang X, Sanderson DJ, Harkness RM, Last NC. Evaluation of the 2-D permeability tensor for fractured rock masses. *Int J Rock Mech Min Sci Geomech Abstr*. 1996;33(No. 1):17–37.
57 Kranz RL, Saltzman JS, Blacic JD. October. Hydraulic diffusivity measurements on laboratory rock samples using an oscillating pore pressure method. *Int. J. Rock Mech. Min. Sci. Geomech. Abstr.* 1990;vol. 27(5):345–352. Pergamon.
58 Fischer GJ. The determination of permeability and storage capacity: pore pressure oscillation method. *Int. Geophys.* 1992;vol. 51:187–211. Academic Press.
59 Fischer GJ, Paterson MS. Measurement of permeability and storage capacity in rocks during deformation at high temperature and pressure. *Int. Geophys.* 1992;vol. 51: 213–252. Academic Press.
60 Larive E. *Etude expérimentale des roches à très faible perméabilité par la mise en œuvre d'un perméamètre de précision*. Institut des sciences de la terre de l'eau et de l'espace de Montpellier; 2002.
61 Bernabé Y, Mok U, Evans B. A note on the oscillating flow method for measuring rock permeability. *Int J Rock Mech Min Sci*. 2006;2(43):311–316.
62 Hadley KH. *Dilatancy: Further Studies in Crystalline Rock*. Doctoral dissertation. Massachusetts Institute of Technology; 1975.
63 Gottschalk RR, Kronenberg AK, Russell JE, Handin J. Mechanical anisotropy of gneiss: failure criterion and textural sources of directional behavior. *J Geophys Res: Solid Earth.* 1990;95(B13):21613–21634.
64 Shea Jr WT, Kronenberg AK. Strength and anisotropy of foliated rocks with varied mica contents. *J Struct Geol*. 1993;15(9-10):1097–1121.
65 Donath Fred A. Experimental study of shear failure in anisotropic rocks. *Geol Soc Am Bull*. 1961;72(no. 6):985–989, 1961.
66 Ramamurthy T. Strength and modulus responses of anisotropic rocks. *Comprehensive Rock Eng.* 1993;1(13):313–329.
67 Nasseri MHB, Rao KS, Ramamurthy T. Anisotropic strength and deformational behavior of Himalayan schists. *Int J Rock Mech Min Sci*. 2003;40(1):3–23.
68 Horn HM, Deere DU. Frictional characteristics of minerals. *Geotechnique*. 1962;12(4): 319–335.
69 Gerrard C. Shear failure of rock joints: appropriate constraints for empirical relations. no. 6. In: *Int. J. Rock Mech. Min. Sci. Geomech. Abstr*. vol. 23. 1986: 421–429. Pergamon.
70 Townend J, Zoback MD. How faulting keeps the crust strong. *Geology*. 2000;28(5): 399–402.
71 Lei X, Masuda K, Nishizawa O, et al. Detailed analysis of acoustic emission activity during catastrophic fracture of faults in rock. *J Struct Geol*. 2004;26(2):247–258.
72 Lockner D. December. The role of acoustic emission in the study of rock fracture. *Int J Rock Mech Min Sci Geomech Abstr*. 1993;vol. 30(7):883–899. Pergamon.
73 Glaser SD, Nelson PP. May. Acoustic emissions produced by discrete fracture in rock part 2—kinematics of crack growth during controlled Mode I and Mode II loading of rock. *Int J Rock Mech Min Sci Geomech Abstr*. 1992;vol. 29(3):253–265. Pergamon.
74 Evans JP, Forster CB, Goddard JV. Permeability of fault-related rocks, and implications for hydraulic structure of fault zones. *J Struct Geol*. 1997;19(11): 1393–1404.
75 Sarout J, Cazes E, Delle Piane C, Arena A, Esteban L. Stress-dependent permeability and wave dispersion in tight cracked rocks: experimental validation of simple effective medium models. *J Geophys Res: Solid Earth*. 2017;122(8):6180–6201.
76 Ahrens B, Duda M, Renner J. Relations between hydraulic properties and ultrasonic velocities during brittle failure of a low-porosity sandstone in laboratory experiments. *Geophys J Int.* 2017;212(1):627–645.
77 Pimienta L, Sarout J, Esteban L, David C, Clennell MB. Pressure-dependent elastic and transport properties of porous and permeable rocks: microstructural control. *J Geophys Res: Solid Earth*. 2017;122(11):8952–8968.
78 Christensen NI. Compressional wave velocities in metamorphic rocks at pressures to 10 kilobars. *J Geophys Res*. 1965;70(24):6147–6164.
79 Walsh JB. The effect of cracks on the compressibility of rock. *J Geophys Res*. 1965;70 (2):381–389.
81 Nishizawa O. Seismic velocity anisotropy in a medium containing oriented cracks. *J Phys Earth*. 1982;30(4):331–347.
82 Cornet FH. *Elements of Crustal Geomechanics*. Cambridge University Press; 2015.
83 Baisch S, Weidler R, Vörös R, Wyborn D, de Graaf L. Induced seismicity during the stimulation of a geothermal HFR reservoir in the Cooper Basin, Australia. *Bull Seismol Soc Am*. 2006;96(6):2242–2256.
84 a Deichmann N, Kraft T, Evans KF. Identification of faults activated during the stimulation of the Basel geothermal project from cluster analysis and focal mechanisms of the larger magnitude events. *Geothermics*. 2014;52:84–97.
b Diehl T, Kraft T, Kissling E, Wiemer S. The induced earthquake sequence related to the St. Gallen deep geothermal project (Switzerland): fault reactivation and fluid interactions imaged by microseismicity. *J Geophys Res: Solid Earth*. 2017;122(9): 7272–7290.
85 Kim WY. Induced seismicity associated with fluid injection into a deep well in Youngstown, Ohio. *J Geophys Res: Solid Earth.* 2013;118(7):3506–3518.
86 Kwiatek G, Martínez-Garzón P, Plenkers K, et al. Insights into complex subdecimeter fracturing processes occurring during a water injection experiment at depth in Äspö Hard Rock Laboratory, Sweden. *J Geophys Res: Solid Earth*. 2018;123(8):6616–6635.
87 Kwiatek G, M, et al. Controlling fluid-induced seismicity during a 6.1-km-deep geothermal stimulation in Finland. *Sci. Adv.* 2019;5(5). eaav7224.
89 Hoek E. Fracture of anisotropic rock. *J S Afr Inst Min Metall*. 1964;64(10):501–523.
90 Donath F. Strength variation and deformational behavior in anisotropic rock. *State Stress Earth's Crust*. 1964:281.
91 McCabe WM, Woerner RM. High pressure shear strength investigation of an anisotropic mica schist rock. *Int J Rock Mech Min Sci Geomech Abstr*. 1975;vol. 12(8): 219–228. Pergamon.
92 Nasseri MH, Rao KS, Ramamurthy T. Failure mechanism in schistose rocks. *Int J Rock Mech Min Sci*. 1997;34(3-4), 219-e1.
93 Cavailhes T, Sizun JP, Labaume P, et al. Influence of fault rock foliation on fault zone permeability: the case of deeply buried arkosic sandstones (Gres d'Annot, southeastern France). *AAPG Bull*. 2013;97(9):1521–1543.
94 Fryer B, Siddiqi G, Laloui L. Compaction-induced permeability loss's effect on induced seismicity during reservoir depletion. *Pure Appl Geophys*. 2019:1–20.
95 Häring MO, Schanz U, Ladner F, Dyer BC. Characterisation of the Basel 1 enhanced geothermal system. *Geothermics*. 2008;37(5):469–495.
96 Hunt SP, Morelli C. *Cooper Basin HDR Hazard Evaluation: Predictive Modeling of Local Stress Changes Due to HFR Geothermal Energy Operations in South Australia*. vol. 16. University of Adelaide Report Book; 2006.